Test setup for LDMX HCal readout

Background and characterisation of polystyrene based plastic scintillator bar containing wavelength shifting fibre

Author
Josh
Greaves

Degree
Bachelor - 4 months half speed

Supervisor
Ruth
Pöttgen

ABSTRACT

It is evident from cosmological observations such as the Cosmic Microwave Background, and the motion of galaxies, that the universe consists of approximately 5 times more mass than visible matter can account for. The Light Dark Matter eXperiment (LDMX) will take a unique approach in its hunt for dark matter; it will look for missing momentum signals in electron collisions with a Tungsten target, and will be looking in the sub GeV energy range for evidence of dark matter interactions. To achieve this, a sensitive hadronic calorimeter system will be required to detect the resulting particles from events that need to be ignored, or vetoed. The basic physical processes that need to be considered for hadronic calorimetry in general, as well as for the hadronic calorimeter in LDMX experiment specifically, are discussed. The experimental setup is presented, consisting of a Styron 665 W Polystyrene based plastic scintillator bar[1], with Wavelength Shifting Fibre (WLS) at the centre, and a Photomultiplier Tube (PMT) at each end. Light output was optimized by grinding the ends of the fibres down, and by increasing the fibre volume inside the bar. Light-tightness was maximised by implementing a simple plastic coupling insert for the fibre, made using a 3D printer. After beta particles failed to produce signals, minimally ionizing cosmic ray muons were used as events to measure the scintillation light in the bar. To achieve this, an area of $\approx 1dm^2$ was covered with overlapping scintillator paddles, which then triggered an oscilloscope to measure the output at the fibre ends. The measured amplitudes were compared to those of apparent single photo-electrons measured by the PMTs.
A basic Python simulation was constructed to attempt to identify parameters that could be optimized for photon collection by the fibre, in slightly different configurations, based on the amount of light that was obtained from cosmic events.
Though there was not sufficient light yield for resolving energies, there was some measurable time resolution. A rough estimate of the event location along the bar axis could be made, which indicated the effective mid point was closer to one end of the bar at $\approx$ 650mm. Finally, an outlook on what the next objectives could be is discussed.

Lund University

FYSK02 - Particle Physics Dept. Conducted: Autumn 2019

Contents

1 Introduction

Of the unanswered questions facing us in elementary particle physics, the question of *dark matter* is high on the list. Cosmological observations have confirmed its existence as a gravitationally interacting material, but the question of where dark matter came from, and its specific nature, still requires an answer. Could dark matter interact with normal matter? Were they coupled somehow at some point in universal history?

To investigate potential non gravitational interactions requires exploration of specific energy ranges. One energy range that has not been explored much at this stage is the sub GeV range, referred to as *light dark matter*. The *Light Dark Matter eXperiment (LDMX)* is an experiment designed to do just that. It is planned to use a high-energy, low intensity electron beam colliding with a fixed tungsten target, and to very closely monitor the momentum exchange of each electron from start to finish. This experiment requires high luminosity, which is a beam characteristic meaning a large integrated number of electrons will be colliding with the target; this leads to high event statistics. LDMX will outperform current fixed target experiments elsewhere in this energy range; it is the first experiment to use the approach of measuring missing momentum, and having 1 or 2 electrons per bunch in the primary beam. With a wide enough beam spot to separate them, these electrons can be precisely tracked even before impacting the target.

Each electron will shower in the Electromagnetic Calorimeter (ECal) after it scatters off the target, and this device will measure the electron's total remaining energy. Any missing energy will be determined here, and could indicate that a dark matter interaction took place. Any events that result from known standard model interactions do not need to be looked at more closely, and can be ignored, or vetoed. Most vetoes will occur in the ECal, but in the case that neutral hadrons are produced by nuclear reactions, an outer Hadronic Calorimeter (HCal) is required to catch and veto those events. A large configuration of plastic scintillating material and dense absorber material with readout electronics will need to be designed, in order to have veto sensitivity to particles from background events.

The aim of this thesis is to setup and calibrate a test readout configuration of a single plastic scintillator bar, with a view to begin preparation for a beam test for LDMX in autumn 2020.

The detector consists of a 1000mm $\times$ 20mm $\times$ 50mm polystyrene based scintillator bar, containing a centralized wavelength shifting fibre to transmit the scintillation light (see later section 2.4, Figure 7). The fibre signals will eventually be read out with silicon photomultipliers (SiPMs), but for this project ordinary Photo Multiplier Tubes (PMTs) are used to gain understanding of the characteristics of the signals due to interactions with beta particles, and cosmic ray muons. Efforts were made to resolve the position along the bar that such interactions take place, where possible.

The relevant physics at work is discussed, including the Standard Model, and how physics beyond the Standard Model leads to motivations for dark matter experiments like LDMX. Relevant interactions between particles and matter are outlined, followed by attempts to optimize the initial lab setup to produce a higher photon yield. A basic toy model simulation has been produced in Python, in order to compare to measured results, and to potentially identify any parameters that could optimize photon yields with the current setup.

2 Motivation and Theoretical Background

2.1 The Standard Model

The details concerning the Standard Model were obtained mostly from Leif Jonsson's lecture notes, from the University of Lund [2]. The Standard Model describes the fundamental particles of nature. These comprise firstly of *fermions*, which obey *Fermi-Dirac statistics*. That is to say, indistinguishable fermionic particles within a system obey the Pauli exclusion principle; one particle cannot occupy the same quantum state as another. Fermions have half integer spin, and exist in three generations of increasing mass. Quarks, which are fundamental fermions, come in six *flavours*; up, down, strange, charm, top and bottom, and these come in three pairs, or three *generations*. Leptons also come in six flavours: the electron, the muon, and the tau particles, which all have the same charge, along with their corresponding neutrinos, which are not charged.

All known matter is made up from fermions, and these particles interact by exchange of *bosons*. Bosons have integer spin, and are nature's mediators of the fundamental forces. Unlinke fermions, they obey *Bose-Einstein* statistics, meaning particles can occupy the same quantum state. The gauge bosons, whose interactions are described by gauge theory, have spin 1, whereas scalar bosons (the only known is the Higgs boson) have spin 0.

The force with the highest coupling strength is the strong interaction. This occurs in two related but distinct levels: first is between the quarks, of which nucleons (baryons) within the atom are comprised, and is mediated by the gluon. Quarks are bound together by these gluons in configurations which are neutral with respect to a charge called the colour charge (distinct from electromagnetic charge). This is so called because three complementary 'colours' are required to neutralize and create a colour neutral particle, the same way red green and blue neutralize to become white. The quarks exchange gluons in their bound states within nucleons. Some residual interaction spreads over the boundary of the nucleons, and manifests as the exchange of mesons (quark-antiquark pairs) between the nucleons. This secondary attraction is what overcomes electromagnetic repulsion between protons to bind nuclei together. It is a residual effect of the fundamental strong interaction between the quarks themselves. Since the mesons are colour neutral, they are observable directly, unlike quarks themselves, but they are unstable and decay quickly.

A unique characteristic of the strong force is that its mediators, the gluons, are also colour charged, which leads them to be self interacting; gluons themselves exchange gluons. This leads to the field between colour charges, such as quarks, to be confined. To illustrate, consider two quarks separated in space. As the separation grows due to energy being added to the two quark system, at some point it becomes more energetically favourable for more hadrons, specifcially mesons which are quark - antiquark pairs, to be produced. This makes it impossible to isolate and observe single quarks. Instead, hadron jets are produced in this process, which is known as hadronization. The *Quantum Field Theory(QFT)* of the strong interaction is known as *Quantum Chromo Dynamics(QCD)*.

In QCD, quantum fluctuations in the vacuum around gluons lead to the production of quark-anti quark pairs which lead to a screening effect with distance. This means that, like in *Quantum Electro Dynamics(QED)*, the interaction grows stronger at short distances; that is, it would, were it not for the fact that gluons self interact, unlike photons. Since the gluons are self interacting, there is another correction to the coupling; If a gluon-gluon pair is produced instead of a quark pair, this leads to an anti-screening effect, meaning the interaction becomes weaker at short distance. This effect is larger than the screening effect in QCD, so the net result is that the coupling is weaker at short distances or at high

energies. This is known as *Asymptotic Freedom*; as the interaction energy is increased, and the distance between particles descreased, the quarks become more *free*. A theoretical state known as *quark gluon plasma* is thought to exist, consisting of asymptotically free quarks and gluons.

Next strongest is the electromagnetic force, which has a coupling strength of approximately $\frac{1}{137}$ times that of the strong force. This force is described completely by Maxwell's equations, which govern the interplay between electricity and magnetism. This is mediated by the massless photon, and every charged particle interacts electromagnetically. Electrons are bound to the protons in atomic nuclei by this interaction. According to Heisenberg's uncertainty principle, the product of a pair of observables in a system must be greater than $\frac{\hbar}{2}$. This applies to the mass energy of a particle, and its lifetime Δt: $\Delta t \propto \frac{\hbar}{\text{mass}}$. Since the photon is massless, its lifetime (and therefore range) is infinite. This is in accordance with the behaviour of electromagnetism in nature. It is also necessary that unlike in the strong interaction, the photon is neutral and so does not self interact. The quantum field theory of the electromagnetic interaction is *Quantum Electro Dynamics(QED)*.

The next force is the weak interaction. There are three associated bosons of the weak interaction; W^+, W^-, Z^0. These bosons are all massive, with masses of $\approx 90\frac{\text{GeV}}{\text{c}}$, unlike those of the other forces. Due again to the uncertainty principle $\Delta t \propto \frac{\hbar}{\text{mass}}$, since their masses are large unlike the massless photon, their lifetimes are very short. It has been found that the weak and electromagnetic interactions are facets of the same fundamental force - the *electroweak interaction*. At a particular energy, known as the electroweak unification energy, they are the same force; the bosons of which are the W^0 and the B bosons. At the unification energy, the Higgs mechanism is required to break this symmetry, which manifests as new bosons comprising a mixture of states of the W^0 and the B bosons. These are the massless photon (γ) of QED, and the Z^0 of the weak interaction. The end result is the electromagnetic force which does not couple to the Higgs field, and the weak force which does. This is what leads to the massive bosons of the weak interaction. In QFT terms, the Higgs field is unique in that it has a non zero vacuum energy, which is responsible for the breaking of electroweak symmetry.

The weak interaction is responsible for nuclear fission, and hence governs radioactive decay. W bosons can cause quarks to change *flavour*. This is how beta decay occurs; a neutron's down quark transforms into an up quark with the release of a W^- boson, and the neutron becomes a proton. For example, in a Strontium-90 nucleus (see section 5.1), one of the neutron's down quarks emits a W^- boson and becomes an up quark. (The Feynman diagram is shown in Figure 29 in the appendix). This three-body decay leads to a spectrum of energies that the beta electron can have, because the total energy is shared with the corresponding electron neutrino that is also produced. The W boson decays into an electron and an electron antineutrino. This electron antineutrino conserves lepton number, since it has opposite lepton number to the electron.

2.2 Dark Matter

In 1933, Fritz Zwicky observed anomalous behaviour among the Coma cluster of galaxies [3]. According to Newtonian mechanics, the Virial theorem relates the time averaged kinetic energy of a mechanical system of particles (or stars/galaxies), to a common central force (such as gravity), where the force is defined by the total potential energy of the

system. In the case of a galaxy cluster like the Coma cluster, this potential is the total gravitational potential energy, which is determined by the total mass in the galaxy.

Observing the redshift of galaxies toward the edge of the cluster, as they moved away from us, he discovered the average velocities were much larger than the Virial theorem would predict. He concluded there must be some *dunkle materie* ("dark matter") hidden from view, contributing a majority of the galactic mass to the cluster.

These observations were supported in the 1970's by Vera Rubin and Kent Ford, using the orbital speeds of spiral galaxies. It became known as the *Galaxy rotation problem* [4]. Since luminous matter becomes more concentrated toward the centre of a galaxy, one would expect the mass to be distributed accordingly. The velocities of the outer stars that were observed were just as high as stars closer to the luminous centre; too high for the galaxies to remain intact, implying the presence of a greater gravitational potential. They concluded approximately six times as much dark mass as luminous mass must be present in these galaxies, though the distribution of the dark matter remains difficult to constrain.

This has been further confirmed by the *gravitational lensing* measurements obtained of intervening galactic masses between here and distant galaxies. As spacetime curves due to mass, the path of light through it also curves, producing a lensing effect around massive objects. The extent of this effect can provide a measurement of the mass of such an object, and has been able to indicate mass to light ratios in agreement with measurements of clusters [5]. All we currently know about dark matter behaviour comes from gravitational evidence.

Quantum Field Theory (QFT) treats all particles as excitements of underlying fields. This includes the bosons which correspond to the fundamental forces. The current state of particle physics research indicates that there may be yet unobserved quantum fields, giving rise to as yet undetected particles, including those responsible for dark matter. This is known as the *hidden sector*, and is supposed to interact with the Standard Model primarily through (but not limited to) gravitation [6]. It is clear that dark matter interacts gravitationally (assuming we have a good current understanding of gravitation), and not electromagnetically (hence *dark*) and it could potentially interact through other forces that are part of this hidden sector. It is in these non gravitational interactions that we hunt for evidence of dark matter.

One long standing candidate for dark matter beyond the Standard Model is the *WIMP - Weakly Interacting Massive Particle*. WIMPs are anything above a few GeV in mass to TeV mass scales. Theoretical extensions to the Standard Model, such as *supersymmetry*, predict WIMP like particles in the mass range appropriate for the current apparent abundance measured for dark matter. Although elegant, supersymmetry is increasingly disfavoured as experiments at CERN's Large Hadron Collider (LHC) have been unable to detect these particles.

Detection of dark matter has been unsuccessful so far through direct and indirect detection; detecting the recoil of Standard Model particles through interactions with dark matter, and the search for decay products such as gamma rays. That leaves fixed target experiments like LDMX, in which dark matter could be produced in collisions of Standard Model particles, and detected that way.

The apparent abundance of dark matter is linked to its behaviour in the early universe, particularly its interaction with standard matter. In fact, the rate of interaction between standard and dark matter could have gone to zero, and the amount of dark mat-

ter could have been *frozen out* at some point, meaning that due to the increasing Hubble expansion rate since the big bang, a point was reached where dark and standard matter became decoupled, leading to a constant relic abundance of dark matter in the universe from that point, which we see today. This is similar to the principle of *photon decoupling*, which occurred around 300000 years after the big bang, leading to the *cosmic microwave background*. In that case, the expansion reached a point where photons ceased scattering with charged particles, and the universe became transparent. This is also the point when *recombination* began, and electrons and protons began forming stable Hydrogen atoms. The scenario of matter and dark matter interacting non gravitationally in the early universe is just one possibility, but it is well motivated and compelling because of its simplicity. Using the current abundance of dark matter, one can work backwards and discover a constrained mass range for possible dark matter particles.

There is a theoretical lower limit to the mass of WIMPs interacting weakly, known as the *Lee-Weinberg bound* [7]. The current dark matter density compared with the annihilation cross section (probability of annihilation) puts this lower limit at $\approx$ 2GeV. One model for *Light* dark matter is based on the supposition that hidden sector dark matter could be coupled to normal matter by a new force, mediated by a *dark photon*. With the presence of such a boson, the self annihilation cross section increases, and dark matter below mass levels of $\approx$ 1GeV becomes viable.

Searching in the light hidden sector is the purpose of the *Light Dark Matter Experiment (LDMX)*, which looks for missing momentum in beam-target collisions to search for evidence of dark matter interactions.

The most stable forms of ordinary matter exist in the mass/energy range of MeV to GeV, which is an energy range that remains largely unexplored for evidence of dark matter. So far, weak boson mediated interactions have been the main focus of experiments, in which dark matter is realized as WIMPs in the GeV to TeV window. Dark matter mediated by hidden sector bosons in the lower mass range could be detected by interaction with electrons. LDMX will leverage this possibility, and by very precisely tracking collisions between electrons with a target, hope to measure missing momentum that will indicate that a dark matter reaction has taken place. The production of a dark particle/anti particle pair, and the production of dark photons which would then decay into dark matter/anti matter pairs (Figure 1), would both have the signature of missing momentum after hitting the target.

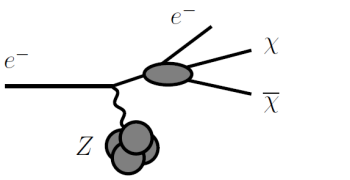

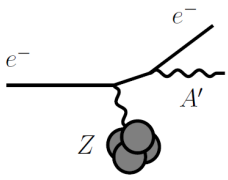

Figure 1: Left: direct dark matter/antimatter production. Right: radiation of a mediator due to dark bremsstrahlung. [8]

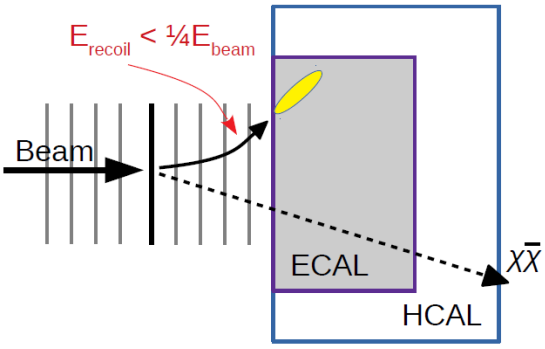

Figure 2: LDMX concept showing electron being tagged and tracked before recoiling off the target after radiating dark matter particles. [8]

2.3 The Light Dark Matter eXperiment, LDMX

According to the experiment design [8], the dominant process being searched for is the production of the dark photon which could decay into a particle antiparticle pair, or secondly, the direct pair production of dark matter particles. Either process will produce a missing momentum signal. A beam of electron bunches, with 1-2 electrons per bunch, delivered at a rate of $\approx$ 40MHz, which is $\approx$ 1 electron every 20ns, will be used, with energy in the range $4 - 16$GeV [8]. Each electron is precisely tagged and tracked in the tagging tracker to the left of the highlighted black target in Figure 2, before impacting the tungsten target. The tracking plates are 10cm separated, inside a 1.5T B-field, which imposes a Lorentz force on the electrons to allow high resolution momentum measurement. They consist of silicon microstrip modules which are sensitive to charged particles, and produce an ionization current as the electrons pass through, with very high spatial resolution. The recoil tracker consists of similar plates, more closely grouped, downstream of the target.

The recoiling electrons are tracked here all the way to the ECal, where they shower and deposit their remaining energy. If the electron has recoiled due to hard bremsstrahlung, then a massless photon has been released, and the electron receives a small kick, or change to its transverse momentum.

Figure 3 shows the fraction of events as a function of electron energy measured in the ECal, for a range of mediator masses. It is clear that the larger the mediator mass is compared to the electron mass, the smaller proportion of the beam energy the recoil electron will have. For Standard Model interactions, the remaining energy of the electron is close to the beam energy, shown in black, and the missing energy will be attributed to any other showering particles in the ECal. For a signal event, the electron loses much more energy, and this effect is larger the heavier the mediator is.

The momentum background is shown on Figure 4, in black on the plot. If a massive particle is released due to dark bremsstrahlung, which is the release of a dark photon instead of a standard photon, then according to the kinematic calculations [8] it receives a larger p_T. Even at low mediator masses, this is very distinguishable from background interactions, and this effect is more apparent the heavier the mediator is. An absence of any particles showering in the ECal besides the electron to account for its missing momentum could identify a signal event.

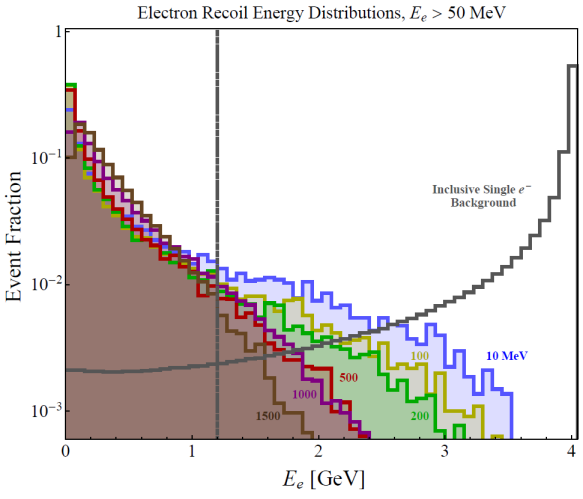

Figure 3: Recoil electron energy distribution for varying mediator masses [8]

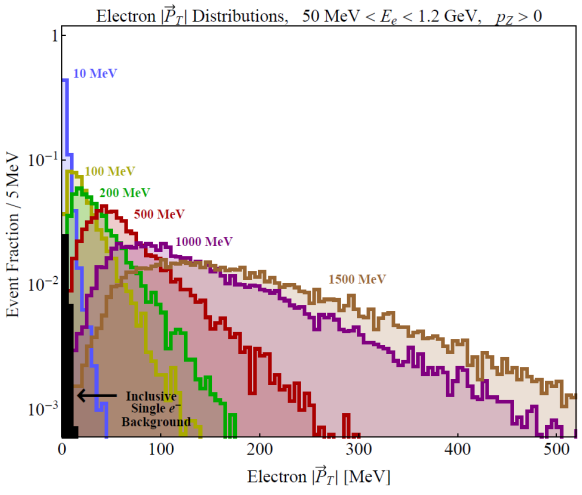

Figure 4: Recoil electron momentum for varying mediator masses [8]

The ECal does not detect all neutral hadrons, muons or other background processes that could possibly be produced by reactions in the target or the ECal itself. These backgrounds comprise a wide range of possibilities, from the most likely; standard *hard* bremsstrahlung producing standard photons, to electro-nuclear reactions, and finally rare photonuclear reactions which can occur in the ECal or in the target, see Figure 6. Nuclear reactions occur when high energy photons or electrons react with the atomic nuclei of the target, or of the detector material, causing the emission of nucleons, or the creation of other particles like pions. The only non measurable background is that of neutrino production, because they interact only by the weak interaction. These events are very rare, but could theoretically contribute to false missing energy signals, creating a false positive. LDMX aims for low enough statistics for such false positive signals not to be an issue.

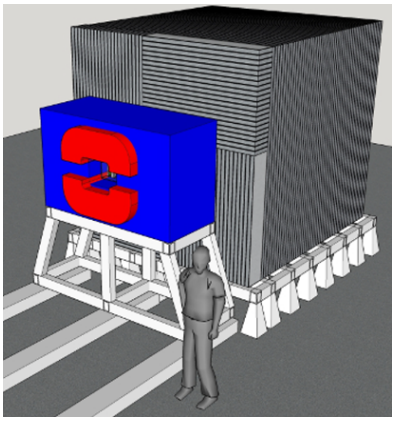

Figure 5: Diagram showing the size and layout of the LDMX detector. [8]

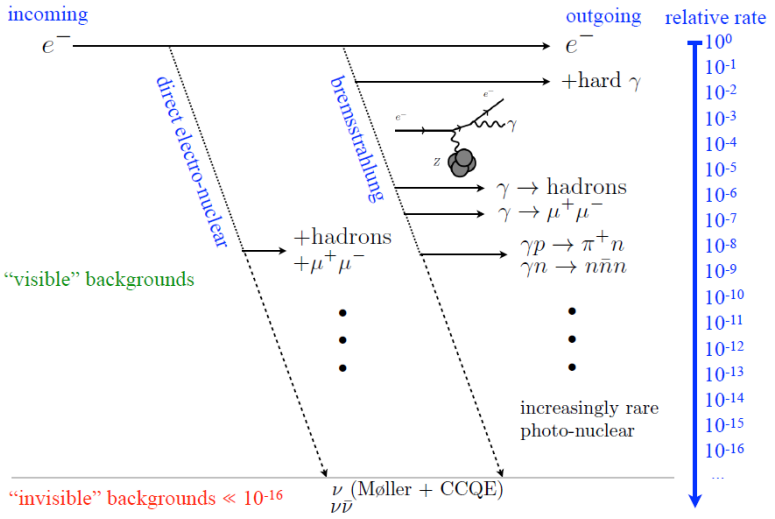

Figure 6: Potential background processes and their relative rates to the number of incident electrons [8]

Sensitivity to all detectable processes is required for LDMX. In order to veto unwanted events, a large HCal system will be required which will sit outside the ECal, to catch any of these decay products, as shown in Figure 5. The plan is to use bars of scintillating material, described in detail below, which will be configured in layers separated by plates of dense absorbing material, such as steel. This is known as a *sampling calorimeter*, as the showering material (steel) is separated from and layered with the scintillating material. Sampling calorimeters are convenient in comparison to *homogeneous* calorimeters in which the entire volume is sensitive scintillator material, because the showering volume (plate thickness) can be varied in comparison to the scintillator bar width. It is now necessary to begin planning more precisely how such a calorimetry system will be designed and used specifically for LDMX.

2.4 Particle and matter interaction - scintillator bar operation

The scintillator bar is a Polystyrene (STYRON 665 W) based organic plastic scintillator, with a TiO_2 coating [1], in order to promote diffuse reflection of light at the bar edges. Plastic scintillators are the most widely used because they are cheap to make and easy to mold compared to some crystal scintillators; inorganic crystal structures must be grown,

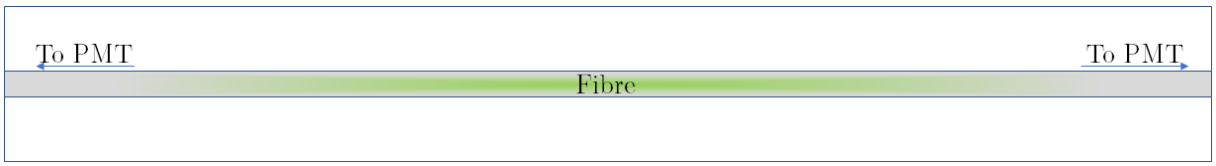

Figure 7: Sketch showing a lengthwise 2D cross section of the bar with the fibre running through the centre.

for example. They also have a fairly good light output - approximately 1 photon per 100eV of deposited energy [9]. This is important for the purpose of hadronic detection in the case of LDMX because the HCal is required only as an event veto indicator. It will require a large volume of scintillator material, and will not be required to resolve energies of event constituents. That task will fall to the EM calorimetry in LDMX. LDMX simply requires the HCal to detect the outcomes of photonuclear events, in order to veto that event and remove it as a dark matter candidate.

Plastic scintillator material exhibits fluorescence which arises from the electronic transitions in the single component molecules. Fluorescence occurs when electrons in higher electronic energy states that have been excited by electromagnetic interaction with charged particles deexcite, and photons characteristic of the energy lost by the electron are emitted. The excitation occurs when an atom absorbs a photon from electromagnetic interaction with the incoming charged particle, which promotes an electron to a higher energy state compared to the ground state, or lowest energy state. The electron then deexcites, but does not release all its absorbed energy at once. It transitions down through intermediate energy states, before returning to its ground state, when a photon is emitted of energy which matches the energy gap of the transition back to ground. Neutral particles, such as neutrons, which are produced as a result of nuclear reactions in the target or the detector, can be detected in LDMX by their interactions with the absorber material separating the calorimeter bars. Secondary charged particles will be produced by nuclear reactions within the atoms of the absorber plates, and these will then cause the downstream bars to scintillate.

Due to the difference between the transition to ground and the photon energy required to excite an electron, the scintillator material is transparent to its own radiation. It emits light at a longer wavelength, and therefore lower energy, than the absorbed quanta. This is due to the energy of the incoming quanta exciting the atom electronically and vibrationally; not all of the initial energy contributes to excitations that lead to radiation when transitioning back down the energy scale. To summarize, photons emitted due to deexcitations will not subsequently be re-absorbed by the material. This transparency is a very important property in scintillator operation; if this were not the case, the signal from deexcitations would be reduced due to photons lost to reabsorption.

As charged particles pass through an interactive material such as a scintillator bar, they deposit their energy at a rate dependent on the *stopping power* of the material itself. Electronic collisions with electrons in the medium, and with atomic nuclei of the material, are responsible for this energy transfer. While the charged particle is traversing the material, it transfers its energy primarily, in our case, to electrons in the molecules, causing the scintillation. The best known approximation for energies in the MeV to GeV range is the *Bethe* formula shown in (1) [10]:

$$\frac{-dE}{dx} = 2\pi N_a r_e^2 m_e c^2 \rho \frac{Z}{A}\frac{z^2}{\beta^2}\left[ln\left(\frac{2m_e\gamma^2 v^2 W_{max}}{I^2}\right) - 2\beta^2 - \delta - 2\frac{C}{Z}\right] \quad (1)$$

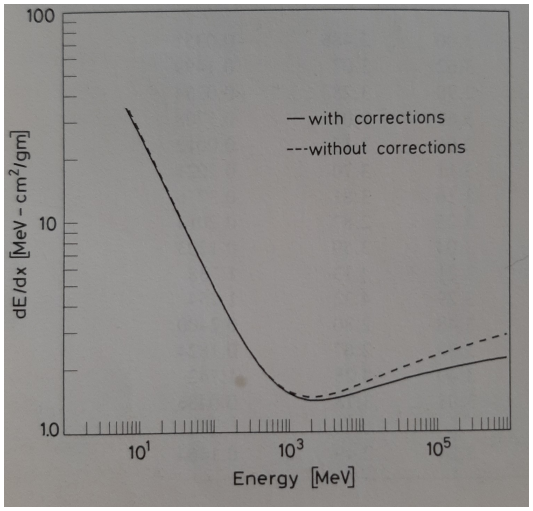

Figure 8: Comparison of the Bethe formula with and without shell and density corrections. This calculation is for copper [10].

r_e:	electron radius
m_e:	electron mass
N_a:	Avogadro's number
I:	mean excitation potential
Z:	atomic number of absorbing material
C:	shell correction
δ:	density correction
A:	atomic weight of absorbing material
ρ:	density of absorbing material
z:	charge on incident particle (units e)
β:	$\frac{v}{c}$ of incident particle
γ:	$\frac{1}{\sqrt{1-\beta^2}}$
W_{max}	max energy transfer (head on collision)
where	$2\pi N_a r_e^2 m_e c^2 = 0.1535$ MeV$\frac{\text{cm}^2}{\text{g}}$

This formulation originated with a classical calculation that assumed an interacting electron with an incoming particle would be at rest compared to the particle. It assumed that the electron would move only very slightly, so that the particle's electric field could be assumed to act only on the electron's initial position, meaning that the formulation would be valid only over a short time, and over a short distance. This formulation did not take into account quantum effects of lighter particles. Hans Bethe used perturbation theory to correct for quantum mechanical effects in calculating the momentum impulse that an electron recieves from an incoming particle, and obtained the formula shown in equation (1).

The first two corrections that were necessary to make, were the *density correction* δ and the *shell correction* C. The density effect is due to the polarization of atoms along the particle's path, due to the electric field of the incoming particle. This has a shielding effect which means that more distant electrons will feel less of the particle's field. As the energy and therefore velocity increase, this polarization effect will become greater. Since a material with higher density means more electrons will feel this effect, it is known as the *density effect*. The *shell correction* comes into effect at the lower end of the energy spectrum; when the orbital velocities of the atomic shell electrons become non negligible compared to the particle velocity, the early assumption of the formula that the electrons are stationary is no longer true.

The curve in Figure (8) is plotted with energy increasing along the x-axis, and the rate of energy transferred or stopping power, on the y-axis. The minimum of this curve is known as the point where the particle is a *minimum ionizing particle*, or *MIP*. The slow rise after this minimum as particles become relativistic, is called the *relativistic rise*, but is mitigated by the density correction as shown in Figure 8. Cosmic ray muons have a short lifetime of $\approx 2 \times 10^{-6} s$ [9]. Due to their relativistic velocity, this lifetime is effectively

extended compared to the lab frame of reference, and they are able to reach the surface of the earth with approximately 4GeV of remaining energy [9]. At this point, they are minimum ionizing, and lose approximately $2\text{MeV}\frac{\text{cm}^2}{\text{g}}$. For the plastic scintillator material, which has a density of $\approx 1\frac{\text{g}}{\text{cm}^3}$ [11], this gives the density independent, linear stopping power as $\approx 2\frac{\text{MeV}}{\text{cm}}$.

To collect the scintillation light and transmit the photons to the PMTs for detection, the Wavelength Shifting Fibre (WLS) is positioned in the centre of the bar. The WLS used is 1.4mm diameter Kuraray double-clad Y11 fibre, which has an absorption peak of 430nm, an emission peak of 476nm and a long attenuation length of > 3.5m [12]; the light is shifted from blue to green. This is achieved using the same principle as the transparency of the scintillator. The fibre material is doped in such a way so that the incoming photons are absorbed and emitted at a longer wavelength; i.e. blue to green. This ensures the photons that reach the photo multipliers are of the same energy, and at an energy that the PMTs are sensitive to, in order to increase the efficiency of photo electron release and signal production.

Treating the light as a wave train of approximate plane waves, when it reaches the boundary of the fibre, it will ideally enter the fibre and be transmitted. However, it may also be reflected. This is due to a principal of optical physics described by *Snell's law*, which relates the relative indices of refraction of two materials, to the behaviour of light at the boundary (equation (2)). The light, which can be approximated as a plane wave locally, travels at a velocity v dependent on the refractive index n of the medium: $n = \frac{c}{v}$. In air, $n = 1$, but the indices of refraction of the fibre and scintillator material are closer to that of polystyrene. At 430nm $n = 1.61 \pm 0.01$ [13].

$$\frac{n_1}{n_2} = \frac{sin\theta_{transmitted}}{sin\theta_{incident}} \tag{2}$$

According to Snell's law, moving to a lower refractive index, such as between the scintillator and the air gap around the fibre, the transmitted angle will be larger than the incident angle; the light bends away from the normal to the surface. Varying the incidence angle to the point where the transmitted angle becomes $> 90°$ is known as the *critical angle*, and indicates the point where no light is transmitted; it is all reflected back into the bar. This indicates that only the light within an acceptable range of incidence angles inside the bar, will be transmitted into the air gap.

Once the light is incident upon the fibre edge, it will be transitioning into a higher index from the air gap. This means that the light will be bent toward the normal, and a greater proportion of the light will be transmitted at this boundary into the fibre itself. The fibre is made up of a core surrounded by cladding with a slightly lower index of refraction, to promote total internal reflection, maximizing transmitted signal. However, the surrounding air gap provides much more of a constraint on the light already in the fibre.

Once the light is internally reflecting inside the fibre, its velocity is determined by:

$$v = \frac{c}{n} = \frac{30\frac{\text{cm}}{\text{ns}}}{1.61 \pm 0.01} = 18.64 \pm 0.12\frac{\text{cm}}{\text{ns}}$$

Its attenuation can essentially be neglected in the case of the length we are dealing with in this experimental configuration. Errors were estimated over the likely range of wavelengths absorbed, based on the fibre absorption spectra [12].

3 Experiment

3.1 Lab Setup

The setup comprised of the scintillator bar at the centre, wrapped in light-tight tape. The fibre ran through the centre of this bar inside an air gap, and protruded from its ends. Each end was optically coupled to the photocathode of a PMT, producing a signal pulse which was read out an oscilloscope channel. As well as this, two paddle scintillators were overlapped, encompassing the bar in between, and were each connected to a (*Nuclear Instrumentation Modules*) NIM discriminator channel to digitize the signal. These digital signals were then passed through a logical AND gate in the form of a NIM coincidence unit, in order to create a trigger signal.

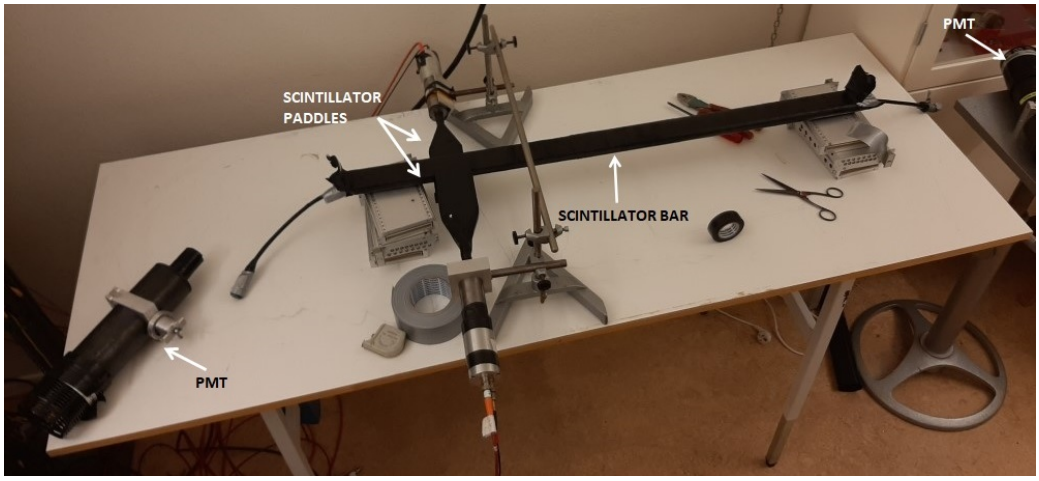

Figure 9: Lab Setup - final setup with reduced fibre length, and 2 fibres in the bar.

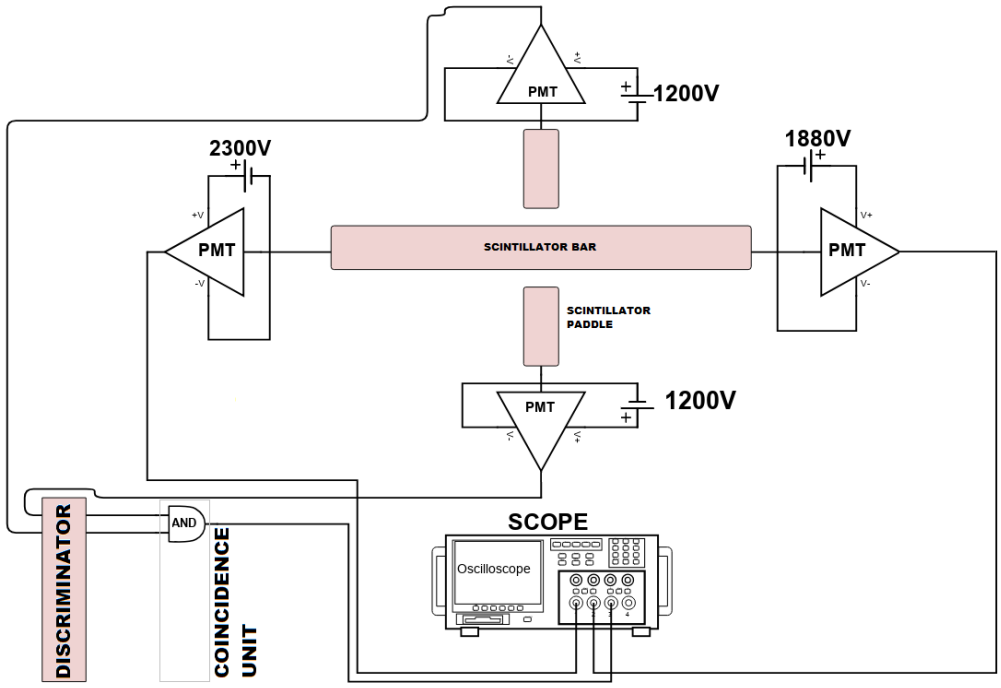

Figure 10: Final, optimized setup schematic - Triggering off the combined signal from paddle scintillators. PMT voltages differ so that their gains more closely match.

To outline the lab setup, Figure 9 shows how the equipment was oriented for the majority of results, and Figure 10 shows a schematic diagram. The disconnected fibre ends are not yet coupled to the PMTs in this image. The specific setup shown was used to observe cosmic muon events, hence the presence of the scintillator paddles to create a trigger signal. Figure 11 shows the NIM used for the logical processing of the trigger

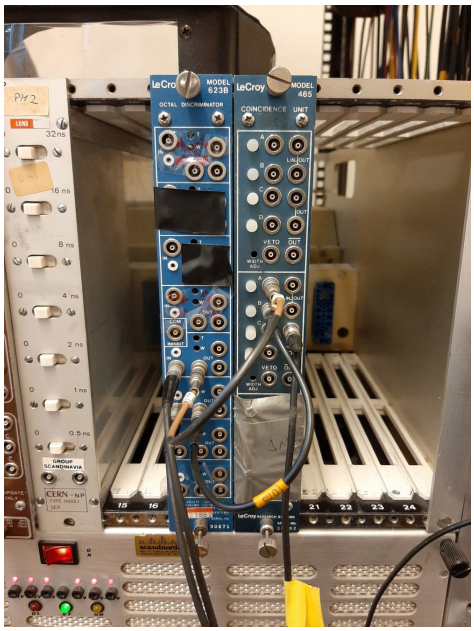

Figure 11: NIM Modules - Discriminator and logical coincidence unit

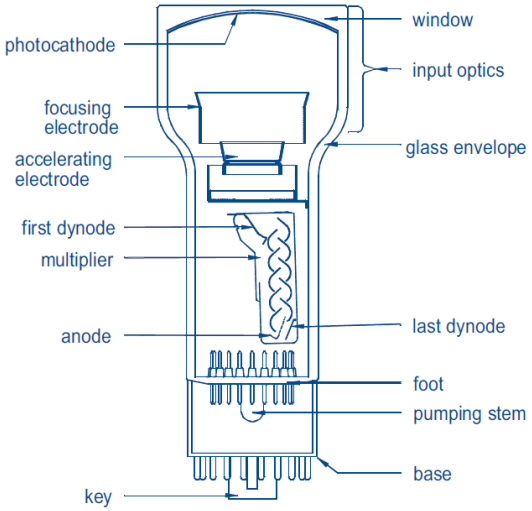

Figure 12: Main elements of a Photomultiplier Tube [14]

signals. NIM is an instrumentation standard widely used in nuclear and particle physics experiments. The discriminator module produces a digital output only when a signal reaches a certain trigger; this is set to 300mV for these channels. The size of the digital output is closer to $1V$. These digital outputs are then fed into the logical coincidence unit which behaves as a logical AND gate. This is how the paddle scintillator signals create a trigger when they are both fired by a cosmic muon event. One paddle is on either side of the bar, so such a signal indicates that some energy must have been depoisted in the bar. In this fashion, we can greatly reduce the amount of unwanted signals on the oscilloscope. The final outputs are connected to the scope trigger, and the analogue outputs from the PMT are connected to the scope channels (Figure 10).

The schematic of an XP2262B PMT is shown in Figure 12. Specific detail of its operation is described later in section 3.2. The schematic in Figure 10 demonstrates how the components are connected together.

3.2 Photomultiplier Tube operation and electronic considerations

Two XP2262B Photomultiplier Tubes (PMTs) are used in this experiment to detect the photons produced by the scintillator bar when energetic particles deposit their energy into the bar material. The first stage of the 51mm, 3×10^7 gain photomultiplier tube, (Figure 12), is the photocathode. The photocathode is made of photosensitive semiconductor material which converts incoming photons into a photoelectrons by means of the photoelectric effect. Due to the quanitzation of photon energy given by the equation $E = h\nu$, if

the wavelength of incoming light is high enough to meet the work function or "threshold frequency" of the photosensitive material required to release an electron from it, then a current pulse proportional to the intensity of incoming photons will be produced at the top of the photomultiplier tube. The kinetic energy of such electrons is determined by the frequency of the incoming light quanta. The spectral response then depends on the the *quantum efficiency (QE)* of the photocathode, defined as the ratio of photoelectrons released to incident photons on the cathode. According to the datasheet for the XP2262B PMTs that were used [14], the QE is determined as shown in the below equation from the quantity *radiant cathode sensitivity (RCS)*, where $RCS = 90_{(\frac{\text{mA}}{\text{W}})}$:

$$\text{QE} = \text{Photon energy} \times RCS_{(\frac{\text{mA}}{\text{W}})} = \frac{\text{hc}}{\lambda} \times RCS_{(\frac{\text{mA}}{\text{W}})} = \frac{\text{hc}_{(\text{eV nm})}}{476_{(\text{nm})}} \times 90_{(\frac{\text{mA}}{\text{W}})} \approx 23.45\% \quad (3)$$

Each photon can cause the release of one electron from the material, provided it meets the threshold frequency. How many of these photoelectrons that are successfully transmitted is what defines this efficiency value.

To detect electrons that are produced by the photoelectric effect as the result of individual incoming scintillation photons, the principle of *secondary emission* is required. If an electron has sufficient energy, it can knock out multiple electrons when hitting a surface. This is where the chain of secondary emission surfaces, or *dynodes*, are introudced. A single photoelectron that has been produced will be accelerated by the electric field in the accelerating electrode toward the first dynode, where it will strike its surface. Provided it has enough initial kinetic energy (dependent on the frequency of the original photon), it will knock out multiple electrons which are then directed and accelerated toward the subsequent dynodes. The total voltage across the PMT tube drops in steps between each dynode, which provides the electric field to accelerate the electrons toward each dynode, and finally the anode. The number of secondary electrons released from a dynode approximates a Poisson distribution to first order, with an average value in the order of 5-10 electrons per incident electron. With a sequence of approximately 10 dynodes, typical PMT's therefore produce a pulse comprising approximately 10^6 secondary electrons at the output.

Most pulses observed across the collected data follow a positively skewed Poisson distribution, due to the fact that the scintillator molecules deexcite in a random and independent way. Within a given time, the number of emitted photons could be expected to approximate a Poisson distribution since the deexcitations happen independently of eachother. That is to say, the average time between photon emissions is known but the exact timing is random. The result of this is that the dynode system is presented with a Poisson distributed collection of photons [15].

There is a saturation point for the incoming electron energy in the release of secondary electrons; the number of electrons excited in the secondary material grows with incoming electron energy, but the atomic depth of these excited electrons also grows. That is to say, the lower the shell of the excited electron, the lower its inherent energy is, and therefore the less likely it will reach energy high enough to be liberated.

4 Simulation

The purpose of this toy model simulation was to first mimic the setup in the lab, before generalizing parameters that would be difficult to adjust in the lab setting. These include things like fibre volume, bar length/geometry, and reflection characteristics and probabilities. The ability to confirm what was seen in the lab, even at a simple level, also helps to confirm understanding of what is happening.

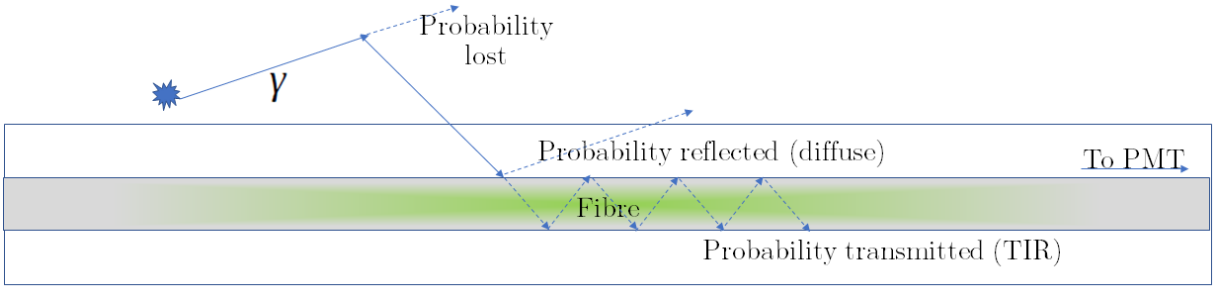

Figure 13: Lengthwise cross section of the bar showing the simulation photon tracking logic.

The logic of the simulation is outlined in Figure 13. Each photon is produced at the assumed location of the event, where it follows a trajectory along a random angle. The photons are individually tracked between their interactions until they are transmitted by the fibre. The probabilities of loss at each interface govern the likelihood that the photons will contribute to the output pulse.

The parameters that can be adjusted include: speed of light in the medium, energy of the scintillation photons, total energy deposited by particles, the total number of photons produced by an event, bar dimensions, fibre volume radius, the PMT output voltage of a single photo electron pulse, the PMT quantum efficiency, and the probabilities of reflection at the bar edges, the bar end, and the fibre surface.
Some simplifications and assumptions made include:

- The simulation currently only reads out photons at one end of the bar
- Each photon scatters diffusely at the edge of the bar, with all angles equally likely.
- Once the photon is inside the fibre, total internal reflection is assumed, and transmission is certain
- The incoming particle deposits all its energy at a single point, and not along a path. Also, a fixed amount of deposited energy is presumed.

The probability of transmission when the photon transitions between the scintillator and the fibre, is also varied. This is used to simulate an air gap, bearing in mind that the simulation does not otherwise model an air gap; the photons go straight from bar to fibre material.

5 Results and Discussion

5.1 Interactions from beta source

To confirm that our configuration could produce a readable scintillation signal through the PMT on the scope, we first elected to use a *beta emitter*. This would provide directed

electrons through the decay of Strontium-90 - a radioisotope of Strontium which fissions due to its instability, producing beta electrons as it does so. These electrons, if of high enough energy, should produce some signal if they can reach the bar scintillator material.

In its first setup configured for measurement of coincident signals with no source present, the system looked similar to Figure 9, but with only a single much longer fibre running through the bar. Our first aim was simply to confirm that we could observe coincident signals in general. We did not yet know the difference in gain between the PMTs, and we wanted to get an idea what was attainable in terms of signal amplitude.

Our first signals were with just one PMT, with light-tight tape sealed around the open end of the fibre. With one fibre input to the PMT of input voltage $2kV$, we sampled at the maximum physical sampling rate of the scope ADC, which is rated at $2GS$/sec across all channels. This upper limit is subject to the ADC clock speed. The time interval between samples was therefore about 1ns per sample.

We used this setup to confirm that we could in fact distinguish peaks on the scope, though we could not yet attribute them to specific scintillation events. To do that, we connected the other fibre end to another XP2262B PMT rated at the same maximum voltage of $2400V$. Once signals were being detected from both ends of the bar, the scope showed a high frequency of events on the trigger channel. Triggering on either channel, it was not possible to pick out conincident events on the other channel from the background.

$$^{90}_{38}\mathrm{Sr} -> e^{-} + \bar{\nu_e} + ^{90}_{39}Y \tag{4}$$

The next step was to introduce a radioactive source to the bar, using a tertiary paddle scintillator placed between the emitter and the bar to trigger the scope. We used a Strontium-90 source, whose sole decay mode is beta decay, at a maximum energy of 546keV. (The decay scheme is shown in Figure 31 [16] in the appendix). After emission from a beta source, free beta electrons are subject to Coulomb scattering (Figure 30 in appendix) dependent on the density of whatever material they are inside, as well as bremsstrahlung as they decelerate. Inside scintillator material, these electrons will begin depositing energy by scattering inelastically with electrons bound to molecules, which begin scintillating. Their deposited energy will be given by equation (1) described earlier. Unable to see anything at all on the scope, the paddle scintillator was removed in order to try to see a difference in one channel, between the presence of the beta emitter at the end of the bar closest to the PMT, and the signal with no source present at all. This was to no avail, as if the beta particles did not have high enough energy to reach the scintillator bar at all. Some of the energy of the emitted electrons would be lost during their journey through the light-tight tape around the bar, and into the bar material itself, but there should not be enough energy lost for them not to cause scintillation at all. The vinyl based tape thickness was $0.5\text{mm} \pm 0.25\text{mm}$, depending on how many layers were used; the particles at the higher end of the spectrum should easily make it beyond a maximum distance of 0.75mm before depositing all of their energy. Given that the maximum energy available from the decay of Strontium-90 is 546keV, which is shared between the beta electron and an electron neutrino (see equation (4)), the maximum kinetic energy the electron can have is 546keV. According to a simulation study carried out at the University of North Carolina Pembroke [17], Figure 32 in the appendix shows the energy distribution of large number of beta electrons emitted during the decay of Strontium-90. The y-axis represents how many electrons there are statistically, as a function of their energy. These electrons are subject to Coulomb scattering off of charged particles in the materials that they pass through. The first material to pass through is the vinyl based electrical tape wrapping the

paddle scintillators and the scintillator bar. Polyvinyl Chloride has a stopping power of ≈ 1.77MeV/cm, which gives an average path length of ≈ 2.3mm [18], assuming a density of 1.25g/cm^3 for the PVC tape. The tape should therefore remove only a fraction of the electron's kinetic energy. The polystyrene base of the bar material has a stopping power of ≈ 1.95MeV/cm $\pm 10\%$ and, assuming a density very close to 1g/cm^3, a path distance of ≈ 2.1mm $\pm$ 10% [18]. The remainder of the beta electron's energy is therefore deposited in the bar.

The conclusion here is that the light yield of this configuration is likely not sufficient to be able to distinguish these events from the background. There must be too high of a loss in terms of scintillation photons escaping the bar, being absorbed by the bar material, or being attenuated in the fibre. There may also be so few photons that, after reflecting multiple times before being transmitted successfully by the fibre, they may appear time shifted enough to be indistinguishable from single photoelectrons being detected by the photocathodes of our PMTs, as opposed to arriving concurrently and generating a measurable pulse.

5.2 Interactions from cosmic rays

The next step was to instead utilize much higher energy, naturally occurring charged particles: cosmic muons. At this point, a second paddle scintillator was introduced as reflected by the lab setup shown earlier in Figures 9 and Figure 10. Now triggering off of the paddle scintillators, a typical output signal obtained is shown in Figure 14.

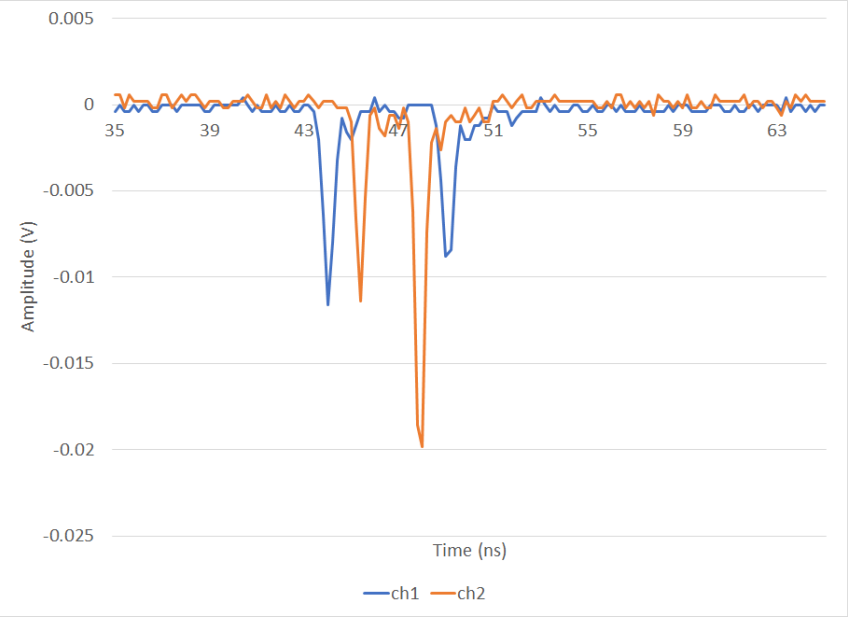

Figure 14: Coincident event at lower amplitude, before optimization, showing potential reflection closer to channel 1.

The peaks are between 10 and 20mV, and it can be seen that this event is closer the the channel 1 end of the bar, as the positioning in Figure 9 shows. The timings of the arrival of each peak could potentially be a result of reflections at one end of the bar, or one end of the fibre. The first peak is on channel 1, followed by channel 2 approximately 2ns later. The next peak is approximately 4ns later than the first channel 1 peak, on channel 2. This could be the result of a reflection from the channel 1 end. Since the speed of light in the bar material is estimated to be $\approx$ 20cm/ns and the bar is 1000mm long, this puts the time for a photon to travel from one end to the other at $\approx$ 5ns in the bar/fibre

material. This is close to what is seen in Figure 14, which shows the signal amplitudes in each channel as a function of time. The sharp peaks represent detections separated in time. The final signal in Channel 1 could potentially be explained by a reflection of the first signal to reach channel 2's photocathode.

To increase the light yield further, a few measures were taken. First, the ends of the fibre were ground down to try to ensure that both ends behaved the same way, and also in an effort to reduce reflections and any lost photons due to scattering off uneven surfaces at the ends. This effort alone resulted in an almost twofold increase in amplitude.

Next, the fibre lengths were matched, so that the propagation time from bar to photocathode were the same for both channels. The fibre was cut down to reduce the overall distance to each photocathode as much as possible. A second fibre was also inserted into the bar, to increase the fibre volume. This again doubled the light yield in a single step.

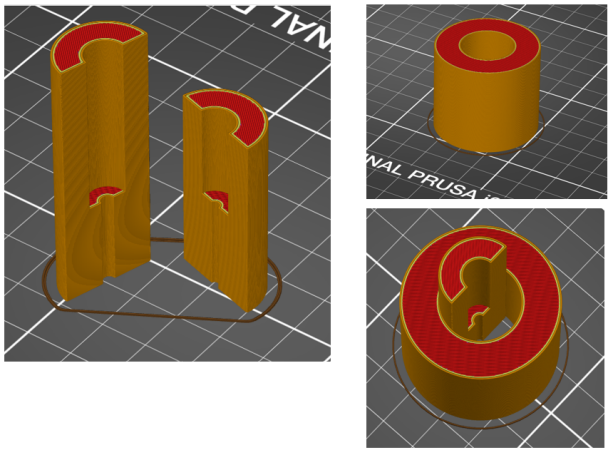

Figure 15: CAD design of photocathode coupler with fibre inserts. Designed in OpenSCAD and presented in Prusa Slicer package which is used to 3D print the piece.

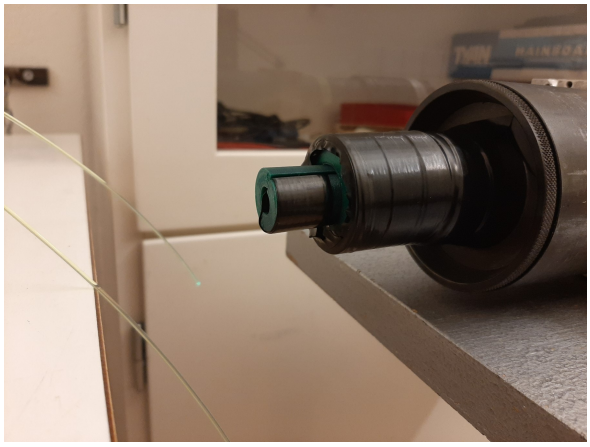

Figure 16: Photograph of the end result of the CAD design - 3D printed on a Prusa i3 MK3S 3D printer

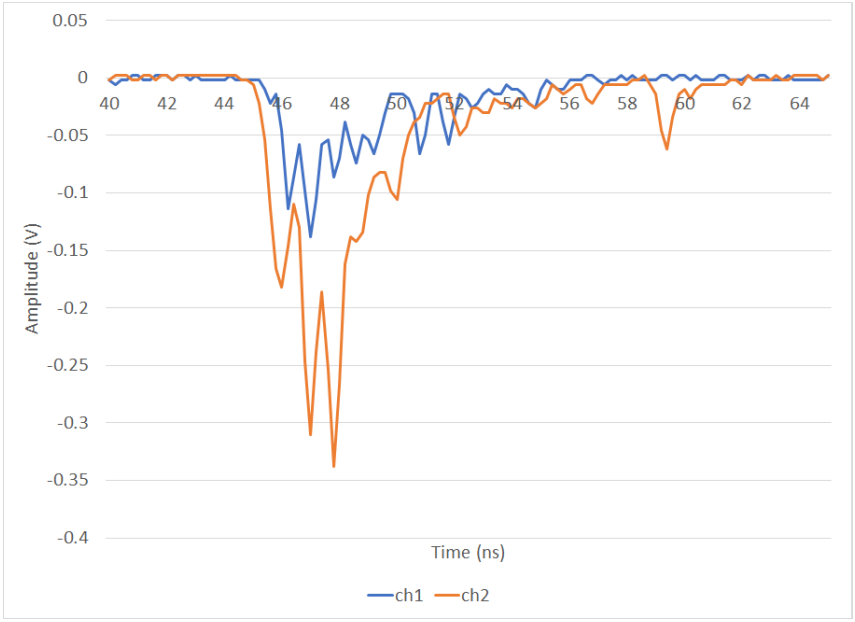

Figure 17: Coincident event at higher amplitude, after optimization before PMT gain matching

Lastly, the coupling of the fibre to the photocathode needed improving. It had not been possible to guarantee that the fibre end would be oriented directly toward the photo cathode. A simple design for a cylindrical coupling at the same diameter as the cathode was designed using an open source package called *OpenSCAD*. This is shown in Figure 15 along side the inserts that were created using the same package. The inserts are two half cylinders which enclose the fibre volume tightly, and are in turn held by the wider hollow cylinder piece flush against the photocathode to ensure maximum light transfer to the PMTs (shown in Figure 16). They are presented here in the *Josef Prusa* [19] 3D printing package which was used to produce the pieces.

Figure 17 shows a typical plot at the current stage of development. The y-axis again shows the signal amplitude in each channel as a function of time. It can be observed that the peak amplitudes are now reaching up to $\approx$ 350mV on channel 2, but significantly less on channel 1. Here it became necessary to match the gain as closely as possible in both PMTs by changing the voltage across each unit.

This was achieved by sampling the output signals for single photoelectron events, and calibrating the voltage across each PMT so that the single photoelectron amplitudes matched as closely as possible. Figures 18 and 19 show signal amplitudes obtained by monitoring each channel, and allowing small amounts of ambient light into the system, downstream from the bar and the fibre. This was in order to search for minimal amplitude pulses for a given voltage. These pulses are then presumed to correlate with the signal produced by a single photon hitting the photocathode (or the minimal stimulus required to cause an electron to be ejected due to the photelectric effect into each PMT).

This process was how the voltages of $2300V$ for channel 1, and $1880V$ for channel 2 were obtained. These voltages are associated with an approximate amplitude of $\approx$ 17mV for each single photoelectron event. Figure 20 then shows pulses from each channel overlapped, now with similar maximum amplitudes. It is clear that the output from channel 2 has more photon content and a stronger and wider pulse overall. This was the result found in the majority of data collected.

The pulse shapes reflect the stochastic process of deexcitation in the scintillator. Figure 21 shows a comparison with the simulation produced; the pulse height is similar, and the distribution in time is a reasonable comparison.

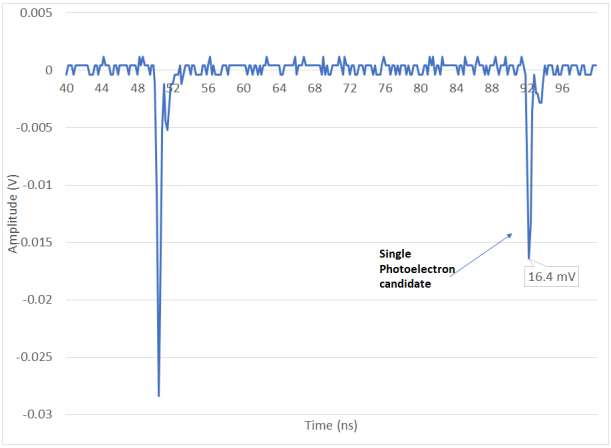

Figure 18: Single photoelectron registering next to a larger signal, on channel 1

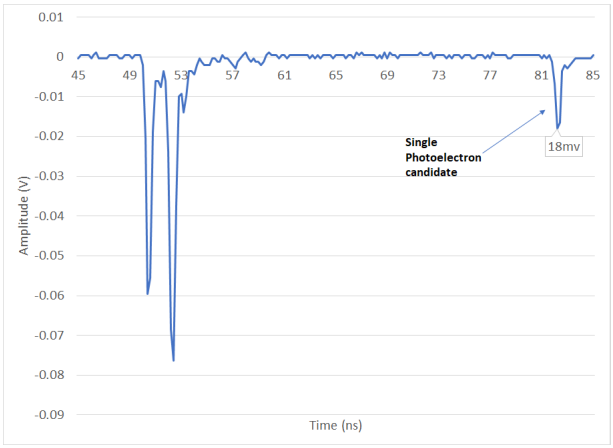

Figure 19: Single photoelectron registering next to a larger signal, on channel 2

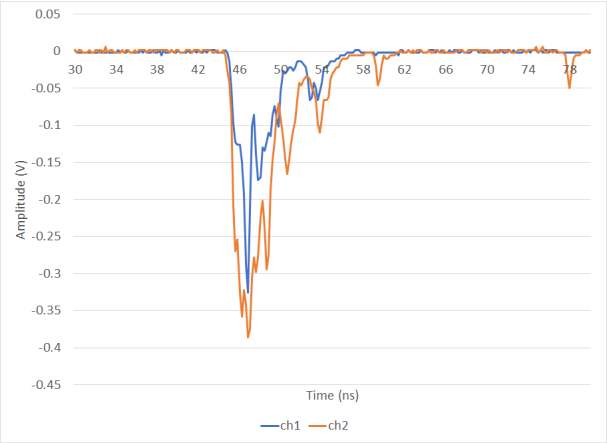

Figure 20: Coincident event at higher amplitude, after optimization and gain matching

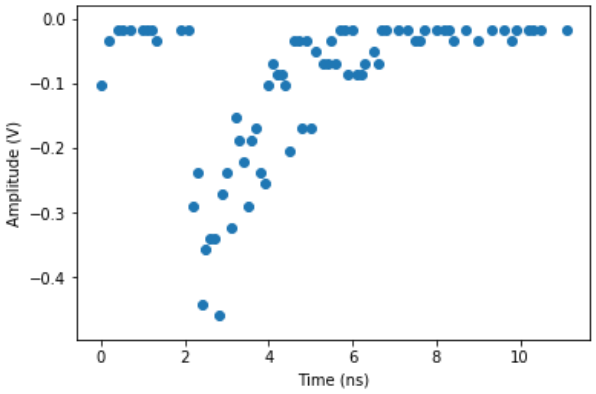

Figure 21: Simulated event for one bar end (see Simulation)

Measurements were again performed in the presence of the Strontium beta source. The efforts were again to no avail, and any events resulting from beta interactions were not distinguishable from the background.

5.3 Simulation Results

Figures 22 through 25 show varying configurations of settings. These include differing the fibre volume and the probability of transmission at the fibre edge. Increasing the fibre volume on its own for example, increases the maximum pulse amplitude, because the likelihood of transmission is higher. This can be seen by comparing Figures 22 and 23. For a lower volume, a given photon has an increased chance to be scattered out of the bar. Increasing the probability of transmission also has a positive effect on the amplitude, since a given photon will have to interact with the fibre less times before it is transmitted. This can be seen by comparing Figure 24 with the other three.

Other parameter settings for these plots are:

- 0% probability of reflection at the bar end - here there is no oxide layer, so the photon is presumed to be lost every time.
- 95% probability that the bar is reflected by the oxide layer - this will likely be close to 100%, but including a slight reduction to simulate any loss.
- 17mV peak voltage of each single photon pulse, from experimental observations.
- Bar dimensions match the lab setup: 1000mm × 50mm × 20mm.

The code for the simulation is available here:
https://github.com/jo6202gr-s/HCal-Simulation/blob/master/SIMULATION.py

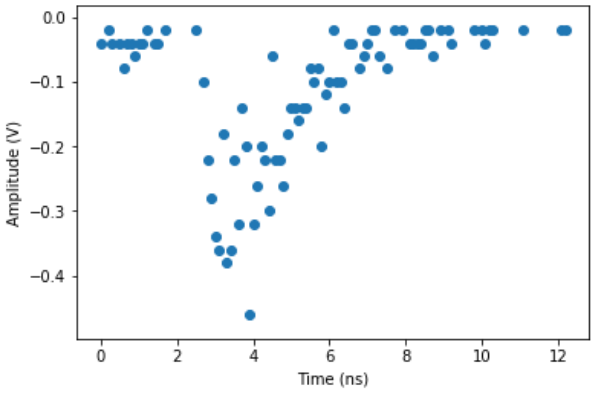

Figure 22: Simulation output for 0.7mm fibre radius, with 25% probability of transmission at fibre edge.

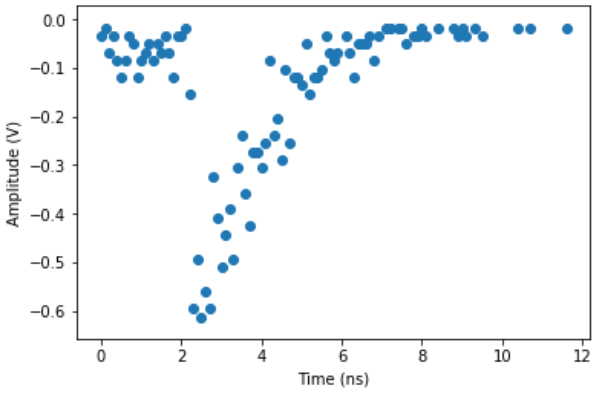

Figure 23: Simulation output for 1.4mm fibre radius, with 25% probability of transmission at fibre edge.

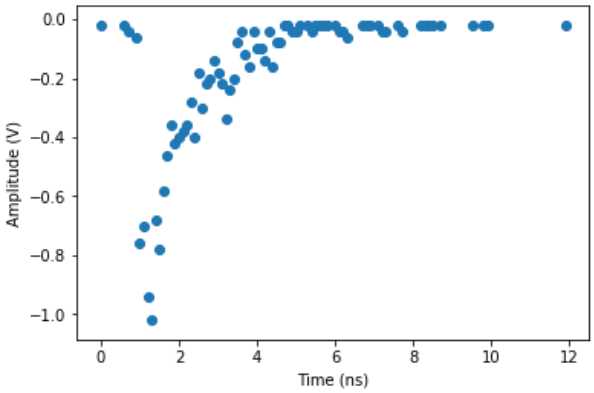

Figure 24: Simulation output for 1.4mm fibre radius, with 75% probability of transmission at fibre edge.

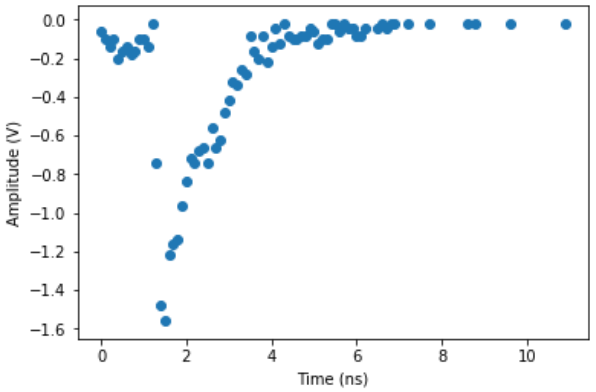

Figure 25: Simulation output for 2.8mm fibre radius, with 25% probability of transmission at fibre edge. Note: Volume modelled as one single fibre, as opposed to two identical fibres side by side, as in reality.

5.4 Position measurements

Figures 26 and 27 show example signals from each PMT output through the discriminator unit. These waveforms have been digitized in order to produce a square pulse to take advantage of the very short rise time. The amplitude of an *ON* signal is $\approx$ 800mV, determined by the NIM discriminator module, which digitizes the signal above a certain threshold trigger, and holds it at that level. These results required some post processing to overcome apparent systematic errors in the discriminator module, in order to isolate as far as possible the absolute time difference between the channels. Offsets for each channel from the scope, to overcome these errors, were as follows: Ch1: $+0.02V$, and Ch2: $+0.092V$. This requirement must be due to some systematic error in the discriminator channels, since this error is not present when reading signals straight from the PMT.

Triggering the scope on the leading edge of these signals makes it a lot easier to accurately observe the time difference between each signal. These show a clear difference of 3ns $\pm$ 1ns at either end of the bar. The large majority of events compared fell within 2-4ns of each other, leading to this error estimate of $\pm$1ns. Figure 28 shows the point at

which the signals arrive completely coincidentally. This point was observed in all cases to be at 650mm $\pm$ 50mm along the bar, which is slightly closer to the channel 2 end in all cases. This error was estimated from observing that the majority of coinciding waveforms occurred between 600mm-700mm along the bar length. The implication of this is that there is some additional delay in the PMT stage at the channel 2 end of the configuration, estimated at 0.75ns $\pm$ 0.25ns. Efforts were made to remove any other differences in delay through each channel. Each NIM unit channel adds approximately 10ns of delay, which was applied to both channels, though some small variation in these channels could also be possible. The cables used were matched for added delay. This same result was obtained using both channels on the oscilloscope, which seems to indicate that any further delay mismatch can be isolated to the channel 2 PMT.

The length of the fibres, after optimization, came to 1400mm $\pm$5mm; 200mm$\pm$5mm protruding from each end of the bar. These errors account for any slight difference from cutting and filing the fibres down. This means that the maximum time from one end of the bar to the opposite PMT, based on a velocity of $v \approx 186.4$mm/ns, would be to the order of 6ns$\pm < 1\%$. All other delays being approximately equal, this should theoretically be the maximum time difference between signals triggered at one end of the bar. The results do not show any higher than a few ns of detectable difference at the extremes, which is within the bounds of this calculation. More precise measurements of refractive indices, to obtain a better constrained value for the velocity, could further reduce this upper bound.

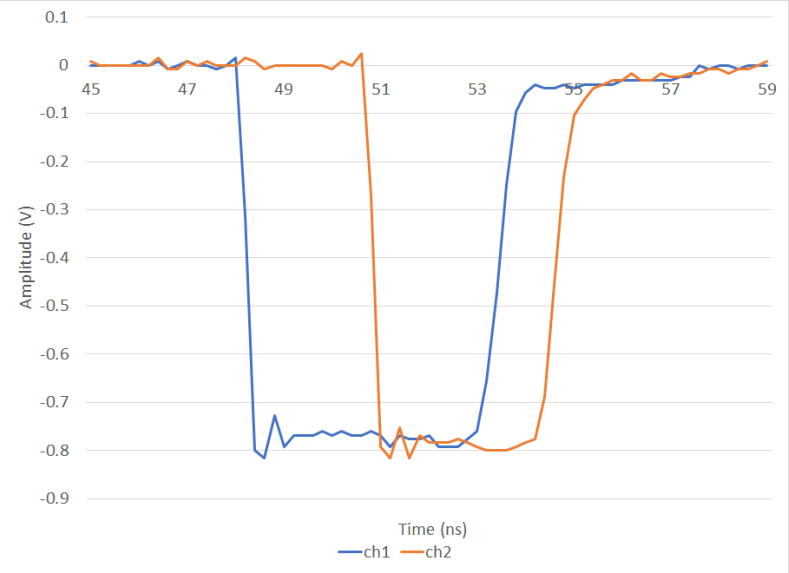

Figure 26: Digitized PMT output signals, triggering on events at the channel 1 end of the bar.

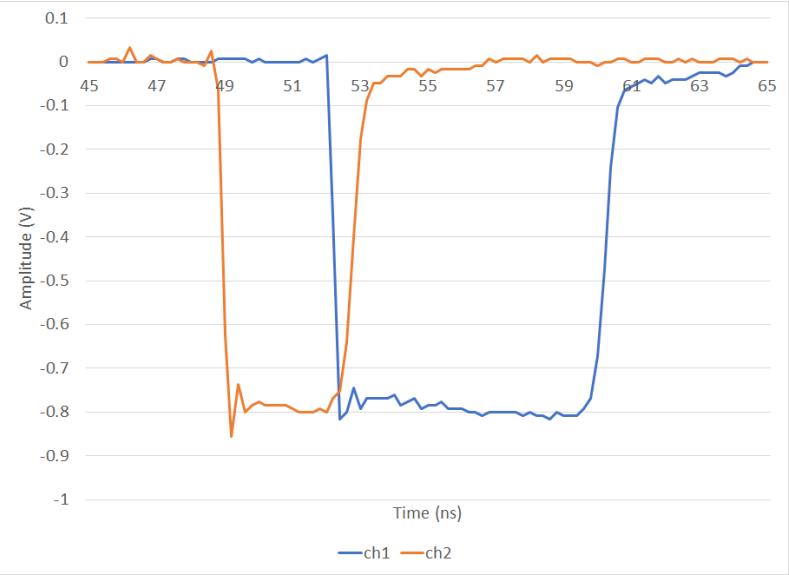

Figure 27: Digitized PMT output signals, triggering on events at the channel 2 end of the bar.

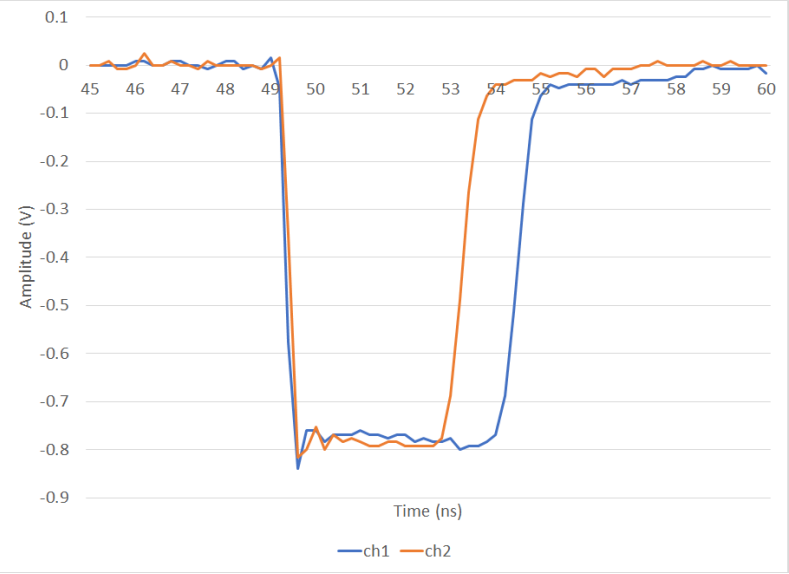

Figure 28: Event triggered at the apparent Mid Point of the system, showing a coincident leading edge of the digitzed waveform from both PMT channels.

6 Conclusions and Outlook

After some improvements to the initial setup, modifications to the fibre and the couplings to the PMTs, a visible signal was successfully obtained from the scintillator bar. There were of course some shortcomings of equipment such as PMT instability and imprecision, and my inability to obtain a visible signal using the beta source. Though the light yield in this configuration was small, and despite the aforementioned shortcomings, it was significant enough to correlate to cosmic ray muon interactions which sent scintillation light to both ends of the bar. I am satisfied that my simulation outputs were representative of the signal outputs I physically observed in the lab. In overall conclusion, this has been a good start to characterizing these scintillating bars. I am confident that the bars are sensitive enough to produce signals of high enough amplitude, from minimum ionizing particles, in order to be able to veto unwanted events in LDMX.

Eventually, many more bars will be used in conjunction with one another, and with a potentially higher fibre volume. One possible configuration is to have two separate fibre apertures at each end of the bars, which will be outputting light to silicon photomultiplier

detectors (SiPMs). As discussed above, the size and placement of these devices will have little to no impact on how the bars are configured, because they are so compact.

The next step in the lab would be implement SiPMs, and to make a comparison of the light output. This would give an idea of how limiting the PMTs used here were. The limiting factors that this would eliminate include all electronic delay and gain differences between the two PMTs. SIPMs are far more compact; they require mounting on some form of small electronic circuit board, but their size is around 3×3mm. They are solid state devices, meaning they operate in the same fashion as a semiconductor; electrons are excited from the valence band to the conduction band of the material. They do not have a sequence of dynodes under a very high voltage in order to accelerate and amplify the photoelectrons, as in the PMT. This means they are not susceptible to magnetic fields, and consume drastically less power. They require a substantial enough electric field to take advantage of *impact ionization*, whereby electrons released by an incoming photon will be accelerated, causing the release of more charge carriers in an avalanche effect. This enables a small optical signal, such as a single photon, to be sufficiently amplified.

The gain of these devices is of similar order to PMTs ($\geq 10^5$) [20], with at least as fast a response time. The band gap of silicon (the energy required to excite an electron to the conduction band) is $\approx$ 1eV. This leads to a high degree of sensitivity for these detectors. Even though my setup was not exposed to any kind of strong magnetic field, there could potentially have been other small environmental effects such as temperature variation, which the SiPMs would not be sensitive to. Silicon PM devices are brand new integrated circuits, compared to the large old PMTs used here. Any electronic noise resulting from the basic operation of a PMT would not be present; the signal from these solid state devices would be expected to be much stronger and cleaner.

Another unknown with these bars is how they age. Recent observations not yet published have seen that the bars age and become less fluorescent, and less effective, at a higher rate than expected. It is not yet known what the root cause of this is, so some testing will be required to fully understand how they will behave and degrade long term. The bars will not be exposed to the brunt of the higher energy ionizing radiation in LDMX, because the HCal will be oriented behind the ECal (Figure 2). However, more knowledge of how the bars may break down due to exposure to high energy electromagnetic radiation will be required.

Improvements that could be made to the logic of the simulation include:

- Introduce a path through the bar dependent on the incident angle of the particle. The length traversed will determine the energy deposited (MeV/cm) (see Figure 33 in appendix)
- More precise modelling of scintillation process; the photon statistics of re emission could be taken into account.
- Consider incident angles of photons for transitions from bar to air, and from air to fibre. Consider the presence of the air gap.
- Currently, the PMT process is not modelled at all. The Poisson distributed response at each dynode could more accurately model the pulse output at the anode.
- Regarding the presentation; each photon should be modelled as a pulse with a non zero width, which superposes with other photon pulses, rather than being binned as a single unit impulse signal.

7 Acknowledgements

Support, guidance and instruction on this project was provided by my supervisor Ruth Pöttgen. I wish also to acknowledge and thank Anders Oskarsson for his support and guidance in the lab, and Geoffrey Mullier for his timely instruction and help in keeping the project moving.

References

[1] Akram Artikov et al. "Photoelectron yields of scintillation counters with embedded wavelength-shifting fibers read out with silicon photomultipliers". In: *Nuclear Instruments and Methods in Physics Research Section A: Accelerators, Spectrometers, Detectors and Associated Equipment* 890 (2018), 8495. ISSN: 0168-9002. DOI: 10.1016/j.nima.2018.02.023. URL: http://dx.doi.org/10.1016/j.nima.2018.02.023.

[2] Leif Jonsson. *Lectures in Particle Physics*. Lund University, 2010.

[3] Heinz Andernach and Fritz Zwicky. *English and Spanish Translation of Zwicky's (1933) The Redshift of Extragalactic Nebulae*. 2017. arXiv: 1711.01693 [astro-ph.IM].

[4] V. C. Rubin, Jr. Ford W. K., and N. Thonnard. "Rotational properties of 21 SC galaxies with a large range of luminosities and radii, from NGC 4605 (R=4kpc) to UGC 2885 (R=122kpc)." In: 238 (1980), pp. 471–487. DOI: 10.1086/158003.

[5] Xiang-Ping Wu et al. "A comparison of different cluster mass estimates: consistency or discrepancy?" In: *Monthly Notices of the Royal Astronomical Society* 301.3 (1998), 861–871. ISSN: 1365-2966. DOI: 10.1046/j.1365-8711.1998.02055.x. URL: http://dx.doi.org/10.1046/j.1365-8711.1998.02055.x.

[6] R. Foot and S. Vagnozzi. "Dissipative hidden sector dark matter". In: *Physical Review D* 91.2 (2015). ISSN: 1550-2368. DOI: 10.1103/physrevd.91.023512. URL: http://dx.doi.org/10.1103/PhysRevD.91.023512.

[7] Benjamin W. Lee and Steven Weinberg. "Cosmological lower bound on heavy-neutrino masses". In: 39.4 (1977), pp. 165–168. DOI: 10.1103/PhysRevLett.39.165.

[8] Torsten Åkesson, Asher Berlin, and et al. "Light Dark Matter eXperiment (LDMX)." In: (2018). https://arxiv.org/abs/1808.05219.

[9] M. Tanabashi, K. Hagiwara, and et al Hikasa K. "Review of Particle Physics". In: *Phys. Rev. D* 98 (3 2018), p. 030001. DOI: 10.1103/PhysRevD.98.030001. URL: https://link.aps.org/doi/10.1103/PhysRevD.98.030001.

[10] W E Leo. *techniques for particle and nuclear physics experiments*. Springer-Verlag, 1987.

[11] *STYRON™ 665 Clear Polystyrene*. Rev. 5.2. Americas Styrenics LLC. Aug. 2016.

[12] Kuraray Corp. *WLS Data sheet*. http://kuraraypsf.jp/psf/ws.html. 2019.

[13] Mikhail N. Polyanskiy. *Refractive index database*. https://refractiveindex.info. Accessed on 2019-12-07.

[14] Photonis Nuclear Instrumentation. *Photonis - Photomultiplier Tubes Catalogue*. http://www.photonis.com. 2019.

[15] E.H. Bellamy et al. "Absolute calibration and monitoring of a spectrometric channel using a photomultiplier". In: *Nuclear Instruments and Methods in Physics Research Section A: Accelerators, Spectrometers, Detectors and Associated Equipment* 339.3 (1994), pp. 468 –476. ISSN: 0168-9002. DOI: https://doi.org/10.1016/0168-9002(94)90183-X. URL: http://www.sciencedirect.com/science/article/pii/016890029490183X.

[16] Brookhaven National Laboratory. *NuDat 2.7 - Data Source: National Nuclear Data Center*. https://www.nndc.bnl.gov/nudat2/reCenter.jsp?z=38n=52. 2019.

[17] Maureen Sikes. *A Monte Carlo Simulation of Energy Deposited in Scinti-Safe Plus 50 by a Charged Particle*. http://www.presentica.com/ppt-presentation/a-monte-carlo-simulation-of-energy-deposited-in-scinti-safe-plus-50-by-a-charged-particle. 2017.

[18] National Institute of Standards and Technology Physics measurement laboratory ESTAR. *Stopping power and range tables for electrons*. https://physics.nist.gov/PhysRefData/Star/Text/ESTAR.html. 2019.

[19] Prusa research Alessandro Ranellucci RepRap. *Prusa Slicer 3D version 2.1.0 +win64*. https://www.prusa3d.com/. 2019.

[20] L. Bartoszek, E. Barnes, and J. P. Miller et al. *Mu2e Technical Design Report*. 2015. arXiv: 1501.05241 [physics.ins-det].

8 Appendix

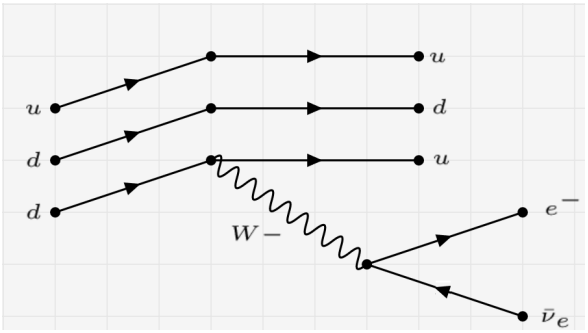

Figure 29: Feynman diagram - beta decay

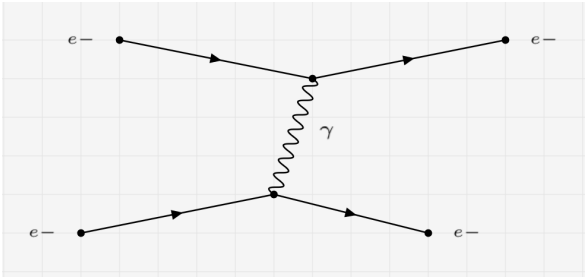

Figure 30: Feynman diagram - Møller scattering between electrons

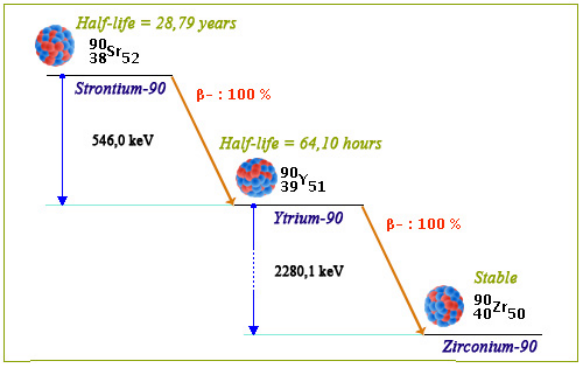

Figure 31: Strontium-90 decay diagram [16]

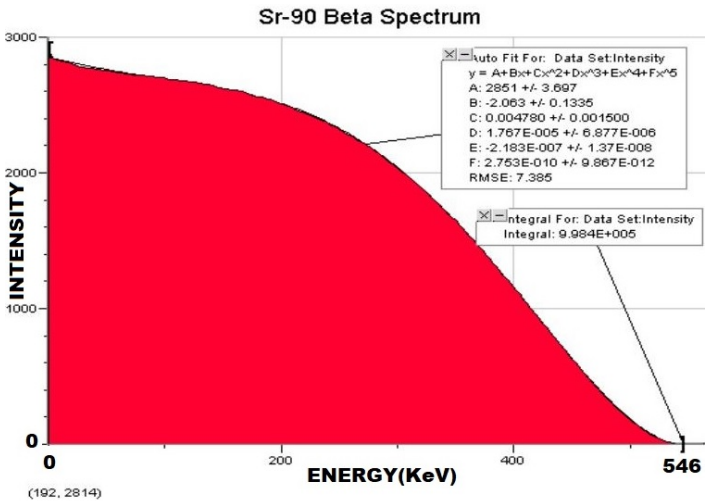

Figure 32: Strontium-90 beta spectrum as modelled by a Monte Carlo simulation

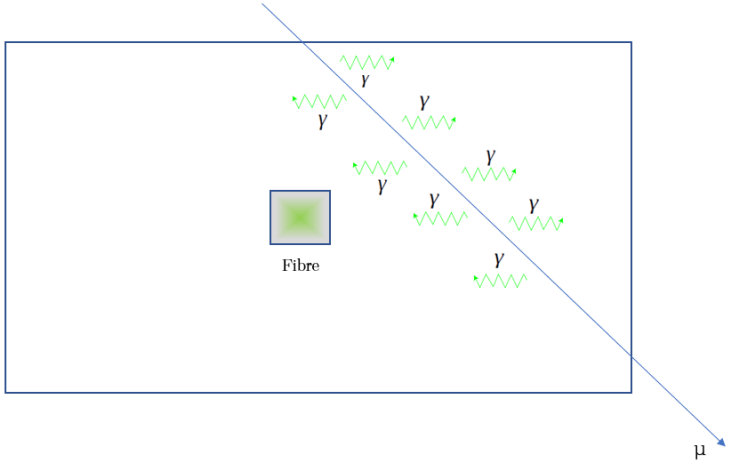

Figure 33: End cross section showing a muon interacting along a path traversed through the bar.